Applied Physics Letters

RESEARCH ARTICLE | OCTOBER 29 2025

Direct observation of the strong thermal non-equilibrium between optical and acoustic phonons in monolayered 2D materials

Special Collection: Advances in Inelastic Light Scattering Spectroscopies

Yu Hua ; Suman Jaiswal ; Masoud Mahjouri-Samani ; Xinwei Wang

Appl. Phys. Lett. 127, 172203 (2025)
https://doi.org/10.1063/5.0299944

AIP Publishing

Applied Physics Letters ARTICLE pubs.aip.org/aip/apl

Direct observation of the strong thermal non-equilibrium between optical and acoustic phonons in monolayered 2D materials

Cite as: Appl. Phys. Lett. **127**, 172203 (2025); doi: 10.1063/5.0299944
Submitted: 29 August 2025 · Accepted: 10 October 2025 ·
Published Online: 29 October 2025

Yu Hua,[1] Suman Jaiswal,[2] Masoud Mahjouri-Samani,[2,a)] and Xinwei Wang[1,a)]

AFFILIATIONS

[1]Department of Mechanical Engineering, 271 ASC 2, Iowa State University, Ames, Iowa 50011, USA
[2]Electrical and Computer Engineering Department, Auburn University, Auburn, Alabama 36849, USA

Note: This paper is part of the Special Topic, Advances in Inelastic Light Scattering Spectroscopies.
[a)]**Authors to whom correspondence should be addressed:** mahjouri@auburn.edu and xwang3@iastate.edu

ABSTRACT

Quantifying thermal non-equilibrium between different phonon branches in supported monolayered two-dimensional materials remains a significant challenge due to complex substrate interactions and optical interference in Raman measurements. Here, we report on the direct quantification of optical-acoustic phonon thermal non-equilibrium in supported monolayered WS_2 materials by leveraging the distinct thermal response of optical phonons (OPs) and acoustic phonons (APs) under modulated laser excitation of different frequencies. The temperature response of different phonon branches is separated based on the measured Raman shift power coefficient (ψ) with high precision. The reduction of the laser spot radius from ~1.7 to ~0.4 μm increases the ψ_{OA}/ψ_{AP} ratio by over 2.5 times, revealing a pronounced enhancement of optical-acoustic phonon thermal non-equilibrium. Comparisons between transferred monolayered WS_2 and hetero-bilayered WS_2/WSe_2 show that the heterogeneous interface strongly strengthens optical to acoustic phonon scattering. In addition, smaller laser spots intensify the hot carrier diffusion effect, reducing the associated OP–AP temperature difference by over 60%. Our method establishes a powerful experimental platform for probing phonon transport in nanoscale materials.

Monolayered two-dimensional (2D) materials, due to their atomically thin nature, present unique challenges for thermophysical characterization.[1] Their low optical absorption requires high laser intensities in Raman-based thermal measurements.[2] Such intense excitation induces pronounced thermal non-equilibrium between optical phonons (OPs) and acoustic phonons (APs), while APs dominate heat transport in 2D systems.[3] This transient OP–AP thermal non-equilibrium[4] can lead to significant errors in measuring thermal properties,[5] yet has been directly quantified in only a limited number of studies.

Our group has developed various Raman techniques aiming to solve this issue. Hunter *et al.* distinguished the OP–AP thermal non-equilibrium and measured the AP-based interfacial thermal resistance (R''_{tc}) of supported monolayered WSe_2 materials based on the frequency domain energy transport state-resolved Raman (FET-Raman).[6] Their model did not incorporate hot carrier diffusion, an important factor strongly influencing local temperature distribution. Our group has developed the energy transport state-resolved Raman technique (ET-Raman) to evaluate the thermal non-equilibrium of few-layered graphene paper,[4] MoS_2,[7] and WS_2,[8] but constraints, including high instantaneous power, long accumulation time, and complex modeling, have limited their suitability for monolayered systems.

In this work, we introduce a FET-Raman method to directly resolve the thermal non-equilibrium between phonon branches in monolayered WS_2. We construct two variables to quantify the OP–AP thermal non-equilibrium under varying laser spot sizes. Also, we refine our physical model by considering the hot carrier diffusion effects and investigate different interfaces' effect on the OP–AP thermal non-equilibrium.

To extract the OP and AP temperatures, our improved FET-Raman method combines temporally modulated Raman measurements by using the distinct build-up times of OP temperature and OP–AP thermal difference. Under laser irradiation, hot carriers in 2D materials are thermalized within picoseconds (ps), subsequently diffusing out of the irradiated region and recombining with holes. Their energy is first transferred to OPs and build up the OP to AP

temperature difference (ΔT_{OA}) on a picosecond timescale, followed by rapid OP–AP energy transport through phonon scattering. ΔT_{OA} is established almost instantaneously, but the AP temperature rise (ΔT_{AP}), which governs heat conduction in 2D materials, evolves much more slowly (from μs to ms). Consequently, when the laser heating cycle is on the order of microseconds or shorter, ΔT_{OA} reaches equilibrium, while ΔT_{AP} remains below its steady-state value. This principle forms the basis of the FET-Raman method in this work. As shown in Fig. 1, a 532 nm continuous wave (CW) laser serves both as the heating source and Raman excitation probe. The measured temperature rise from the Raman shift (pink curve) has combined contributions from both ΔT_{OA} and ΔT_{AP}, whereas the blue curve is only for ΔT_{AP}. The laser passes through an electro-optical modulator to obtain an amplitude-modulated laser beam. Note that as the CW laser source does not change, the modulation frequency only affects ΔT_{AP} rather than ΔT_{OA}. Therefore, when the modulation frequency increases, ΔT_{OA} remains the same, while ΔT_{AP} gradually drops down due to its slower thermal response, and finally converges to half of ΔT_{AP} under the CW case ($\Delta T_{AP,CW}$).

Three supported samples with different configurations (an as-grown, a transferred monolayered WS_2 sample, and a hetero-bilayered WS_2/WSe_2 sample) are prepared. The fabrication and characterization details of them can be found in Sec. S1 and Fig. S1 of the supplementary material. The FET-Raman measurement is conducted on the above-mentioned WS_2 materials. Similar as our work reported before,[9] a 532 nm continuous wave (CW) laser is used to heat the sample and excite the Raman signal. Three objective lenses (20×, 50×, and 100×) are introduced to produce different scales of space heating profiles. Under each objective, five different temporal heating states including one steady state under CW irradiation and four transient states at 10, 15, 20, and 25 MHz modulations are generated. To ensure the accuracy of our measurement, all the modulated waveforms are calibrated to be 50% duty cycles with zero offset and verified through a high-speed photodiode. The Raman spectrum under each heating state is recorded at room temperature under eight laser power levels and then fitted to obtain the temperature-related Raman shift power coefficient (RSC, denoted as $\psi = \partial\omega/\partial P$, cm^{-1}/mW). We use a cross correlation method to fit the Raman spectrum under various power levels to obtain $|\psi|$, which is less affected by data fluctuation compared with the traditional Raman peak fitting.[10] Figure 2 shows a case of test results based on the above-mentioned steps. Specifically, the objective lens used is 20×, and the laser spot radius is 1.8 μm. The test sample is hetero-bilayered WS_2/WSe_2 material mentioned earlier. From Figs. 2(a)–2(d), the modulation frequencies are 0 MHz (CW), 25 MHz, 20 MHz, and 10 MHz, respectively. Although the laser power in all the heating states shown here is the same, as we set the duty cycle of modulation as 50%, the Raman spectrum intensity under the CW case reaches about twice as much as the others. Also, in three transient heating states, the higher magnitude of RSC corresponds to a lower modulation frequency, but all the magnitudes of RSC in transient states are larger than half of that in the CW case, which confirms the rationality of our theory mentioned before about the OP–AP thermal non-equilibrium.

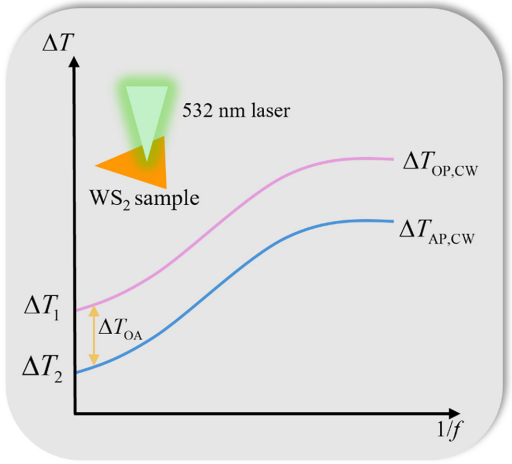

FIG. 1. The schematic of our FET-Raman method. As f increases, the temperature rise induced by APs (ΔT_{AP}) gradually decreases (blue curve), ultimately approaching ΔT_2 with $\Delta T_2 = 0.5\Delta T_{AP,CW}$. However, due to the presence of ΔT_{OA}, the temperature rise induced by the modulated laser ΔT_{OP} (pink curve) ultimately approaches $\Delta T_1 = \Delta T_2 + \Delta T_{OA}$, exceeding 50% of $\Delta T_{OP,CW}$, and we have $\Delta T_{OA} = 2\Delta T_1 - \Delta T_{OP,CW}$.

Figure 3 comprehensively shows the FET-Raman test results of hetero-bilayered WS_2/WSe_2 materials. For each modulation frequency, we do 5–8 measurements and get the average of RSC as the final value. It can be seen that because of localized heating, under the same modulation frequency, with the laser spot size decreasing, the $|\psi|$ magnitude increases. The $|\psi|$ magnitude under infinite modulation frequency is obtained by extrapolating the test results to the 0 limit of $1/f$. Due to the limitation of our optical–electrical modulator, 25 MHz is the highest laser modulation frequency we can reach. Still, the current four data points are sufficient for fitting to capture the extrapolation value. The rationality of it is confirmed by our recent work,[11] in which we build an exact physical model to simulate the relation between 2D materials' temperature rise and $1/f$, and the results show that the extrapolation value based on the ΔT_{AP} of 10, 15, 20, and 25 MHz agrees well with the expected $0.5\Delta T_{AP,CW}$. The ratio between extrapolation temperature rise and the measured temperature rise under the CW case is not affected by defects and OP relaxation time, as the laser irradiation profile remains the same in the CW state and the four transient states. Note that such mathematical extrapolation does not correspond to a physically realized steady state at the infinity modulation frequency. Actually, our FET-Raman is only applied for situations in which the laser modulation period is much longer than the hot carrier and OP lifetime, so that the OA thermal non-equilibrium is effectively frequency-invariant across the transient modulation. It is important to note that the relation between $|\psi|$ and $1/f$ would vary under different scales of laser irradiation. We apply different fitting models to get the extrapolation of the data under different laser spot sizes. Under the 20× objective, the linear fitting method is enough to capture the relation between $|\psi|$ and $1/f$ [Fig. 3(a)]. Under 50× objective, with the increase in $1/f$, $|\psi|$ grows rapidly at the beginning, and then this growth rate gradually diminishes. To capture this change, the combination of linear fitting and exponential fitting methods is applied. As shown in Figs. 3(b) and 3(c), the experimental data are fitted using a linear and an exponential function, and the final extrapolated value is the average of the two intercepts by these two methods. Under 100× objective, the laser heating region becomes highly localized, and the growth of $|\psi|$ becomes larger when $1/f$ increases. In this case, the

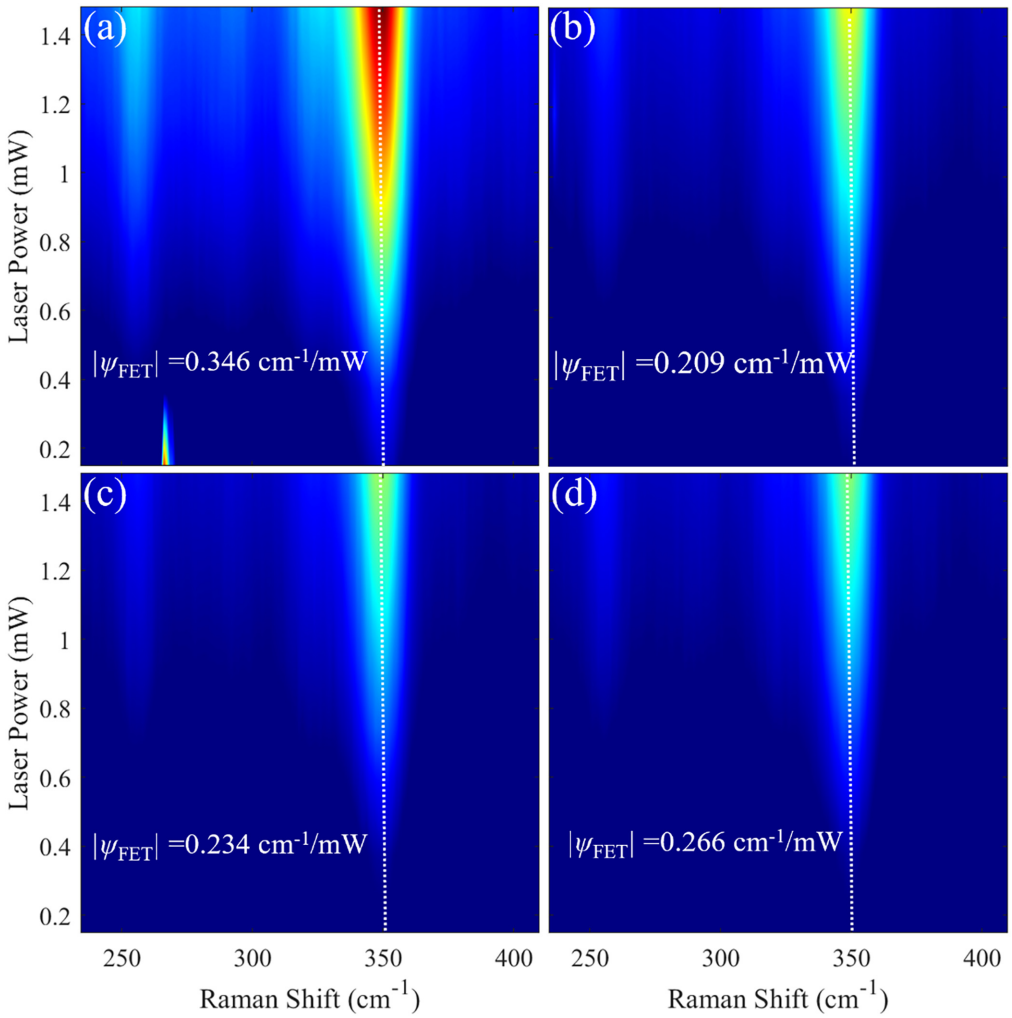

FIG. 2. Contour maps of the Raman spectrum of the E_2g mode measured for the hetero-bilayered WS_2/WSe_2 sample for CW (a), 25 MHz (b), 20 MHz (c), and 10 MHz (d) modulated laser.

extrapolation value is obtained through fitting the experimental data solely based on the exponential function. The detailed fitting and calculation results of all the samples are shown in Table S1. For convenience, we use the absolute value of ψ, while its true value is negative.

Figure 4(a) presents a comparative analysis of ψ_{OA}/ψ_{AP} under different objectives to directly show the OP–AP thermal non-equilibrium. When the laser spot radius decreases from ~1.7 to ~0.4 μm, ψ_{OA}/ψ_{AP} of the hetero-bilayered WS_2/WSe_2, transferred monolayered, and as-grown monolayered WS_2 materials increases by 2.63, 2.73, and 3.78 times. This observed inverse relationship between the laser spot size and ψ_{OA}/ψ_{AP} reflects a fundamental shift in the degree of OP–AP thermal non-equilibrium. Such observation can be rationalized by considering the spatial coupling characteristics of hot carriers and phonons. Under laser irradiation, the photon energy is transferred from hot carriers to OPs, and then to APs. The hot carriers are rapidly thermalized by the absorbed photons, diffuse through the concentration gradient, and then transfer the energy to the OPs. The OPs serve as energy intermediaries to rapidly transfer the absorbed photon energy out, for their limited lifetime and negligible contribution to heat conduction. Therefore, the spatial extent of their energy influence is thus largely determined by spatial distribution of extended hot carrier diffusion length Δr_1, which can be expressed as $\Delta T_{OA} \propto (\Delta r_1 + r_0)^{-2}$, where r_0 is the laser spot radius. However, the temperature rise of APs is affected by both hot carrier diffusion and intrinsic phonon scattering, enabling them to spread energy over a larger region Δr_2, which can be expressed as $\Delta T_{AP} \propto (\Delta r_2 + r_0)^{-2}$, where $\Delta r_2 > \Delta r_1$. Consequently, $\Delta T_{OA}/\Delta T_{AP}$ scales with $(\Delta r_2 + r_0)^2/(\Delta r_1 + r_0)^2$. If r_0 decreases, this ratio increases, leading to a higher $(\Delta T_{OA}/\Delta T_{AP}) \propto (\psi_{OA}/\psi_{AP})$. This is aligned with the observed enhancement in the OP–AP thermal non-equilibrium for tightly focused laser excitation. While for larger spot sizes, the spatial gradient diminishes, and the system approaches a quasi-local thermal equilibrium regime where ΔT_{OA} becomes negligible relative to ΔT_{AP}. Therefore, the measured $|\psi|$ can be more accurately interpreted as representing the AP temperature alone.

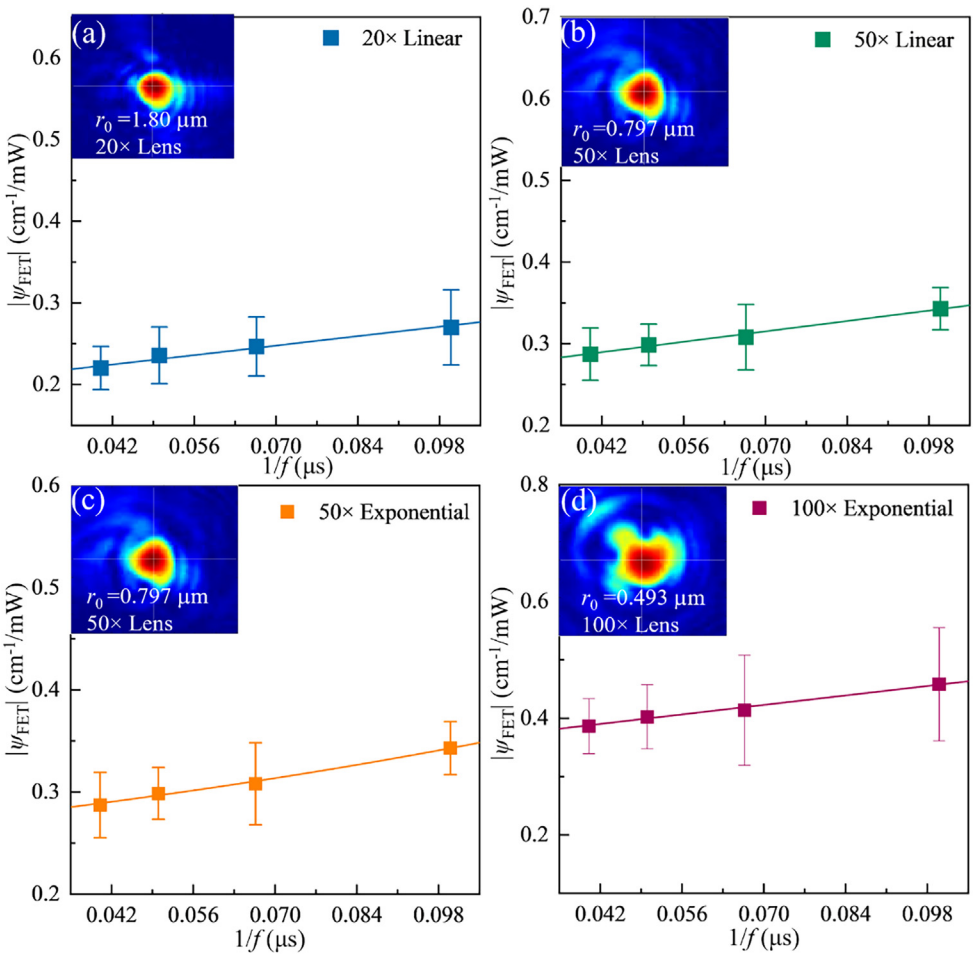

FIG. 3. Fitting to determine $|\psi|$ induced by ΔT_{OA}, and the corresponding laser spot image. Under 20× objective (a), 50× objective (b, c), and 100× objective (d).

It is critical that the hetero stacking of different 2D materials largely affects the OP–AP thermal non-equilibrium. In Fig. 4(a), for the sample of transferred monolayered WS_2, the ratio ψ_{OA}/ψ_{AP} under 100× (0.456 μm), 50× (0.872 μm), and 20× objectives (1.837 μm) are about 71%, 45% and 20%, respectively. For the hetero-bilayered WS_2/WSe_2, the ratio ψ_{OA}/ψ_{AP} under three different objectives (0.493, 0.797, and 1.800 μm) are about 41%, 30%, and 11%. Comparing the ψ_{OA}/ψ_{AP} of the two WS_2 samples under the corresponding objective, the ψ_{OA}/ψ_{AP} values of the transferred monolayered WS_2 is larger than those of the hetero-bilayered WS_2/WSe_2 sample. This can be attributed to the reduced R''_{tc} from more intensive van der Waals coupling at the WS_2/WSe_2 interface,[12] which can facilitate more rapid energy transfer between the OPs and APs and thus decrease ΔT_{OA}.[13]

The R''_{tc} of the three WS_2 samples are extracted using our established 3D numerical model[14] combined with Raman measurements.[15] Briefly, we determine the normalized theoretical and experimental $|\psi|$ values, $\theta_i(R''_{tc})$ and $\theta_{i\,exp}$, based on $\theta = \psi_{AP,FET}/\psi_{AP,CW}$ under the 20× objective and 25 MHz modulation frequency to suppress the effect of the hot carrier diffusion and in-plane heat conduction,[16] with the input including the in-plane thermal conductivity of 28 W/mK[17] and the hot carrier diffusivity of 2.0 $cm^2 \cdot s^{-1}$ for the monolayered WS_2.[18] Note that we adopt an effective treatment $\rho c_{p,effect} = (\rho c_{p,WS_2} \cdot \delta_{WS_2} + \rho c_{p,WSe_2} \cdot \delta_{WSe_2})/(\delta_{WS_2} + \delta_{WSe_2})$ for the hetero-bilayered WS_2/WSe_2 case, where δ is the material's thickness, to address the R''_{tc} contribution from the WSe_2/SiO_2 interface. A probability distribution function incorporating the experimental uncertainty (σ_i) is then constructed: $\Omega = \exp[-(\theta_i(R''_{tc}) - \theta_{i\_exp})^2/2\sigma_i^2]$. When $\Omega = 1$, the optimized R''_{tc} of the hetero-bilayered WS_2/WSe_2, the transferred WS_2, and the as-grown WS_2 are determined as 4.8×10^{-6}, 3.94×10^{-5}, and 8.5×10^{-6} $K \cdot m^2 \cdot W^{-1}$, respectively. Notably, the smaller R''_{tc} of the hetero-bilayered WS_2/WSe_2 and the as-grown WS_2 directly reflects the improved interface contact, indicating stronger interface energy coupling.

We further evaluate the energy coupling coefficient G_{OA} between OPs and APs from the approximate relation: $G_{OA} \approx (\psi_{OA}/\psi_{AP})^{-1} \cdot G_{int}/\delta_{WS_2}$[4] with $G_{int} = 1/R''_{tc}$ and $\delta_{WS_2} = 0.618$ nm.[19] G_{OA} of the hetero-bilayered WS_2/WSe_2, the transferred monolayered WS_2, and the as-grown monolayered WS_2 materials are 2.96×10^{15}, 2.15×10^{14}, and 1.33×10^{15} $W \cdot m^{-3} \cdot K^{-1}$, respectively. The G_{OA} of the three WS_2 samples show the same

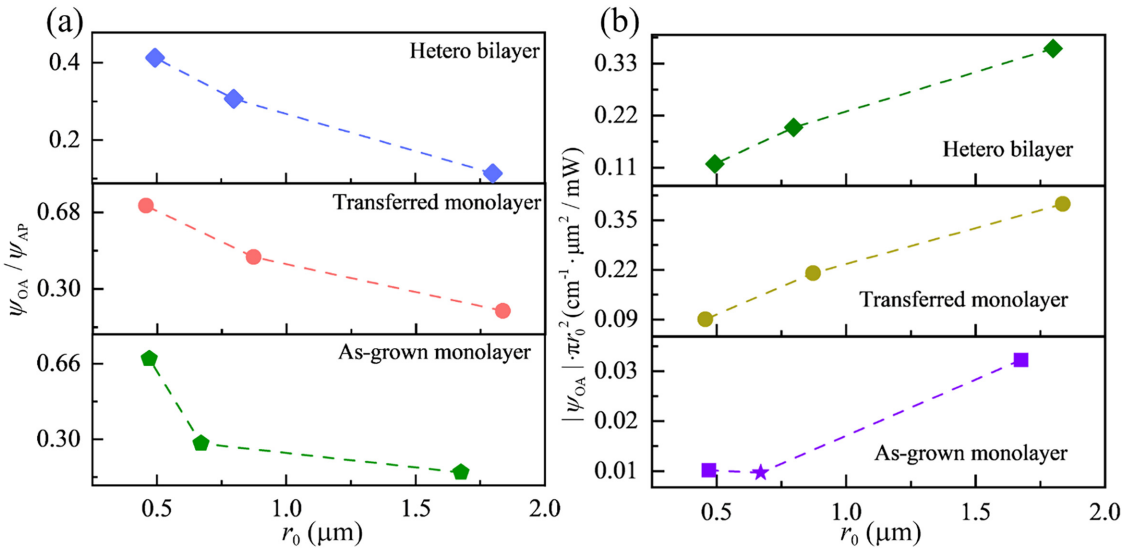

FIG. 4. (a) Dependence of ψ_{OA}/ψ_{AP} on r_0 for the three different WS_2 samples. (b) Dependence of $|\psi_{OA}| \cdot \pi r_0^2$ with r_0 for the three different samples.

order of magnitude as our previous works.[8] It has been documented that $G_{OA} \sim C_{ph}/\tau$,[20] where the phonon heat capacity C_{ph} is not easily affected by the substrate, while the phonon's relaxation time τ is strongly influenced by the substrate.[21] The measured G_{OA} reveals that the OP's relaxation time decreases sequentially from the transferred monolayered WS_2 to the as-grown monolayered WS_2 and further to the hetero-bilayered WS_2/WSe_2. This trend indicates that the stronger interface coupling gives rise to better interface contact, which causes more OP scattering, thereby reducing the OP's relaxation time. Note that external defects, strain, and contamination may reduce the lifetime of hot carriers and phonons, shifting the magnitude of ψ and R''_{tc} across multiple flakes. Here, we treat them as covariates, interpreting the case-by-case variations in G_{OA} across multiple flakes with the same layer configuration. From our experience, the reproducibility of results in suspended samples is better with more uniform geometry and reduced interfacial disorder.[18]

The $|\psi_{OA}|$ in our work encapsulates an ensemble-averaged temperature difference between overall OP and AP branches, rather than pinpointing the dynamics of any specific phonon mode. Due to the ultrafast relaxation timescales within each phonon branch, we assume that intra-branch thermal equilibrium shares a common effective temperature.[22] This simplification allows us to treat the OP–AP temperature disparity as a scalar metric of the average non-equilibrium, which is especially practical for interpreting experimental Raman data that are insensitive to individual phonon modes but are influenced by their collective behavior.

To elucidate the spatial influence of laser spot size on the degree of OP–AP non-equilibrium, we compare a parameter $|\psi_{OA}| \cdot \pi r_0^2$ under different laser spot sizes of the three WS_2 samples. $|\psi_{OA}| \cdot \pi r_0^2$ characterizes the extent of the OP–AP temperature difference under unit laser irradiation per unit area, which reflects the optical phonon energy retention under standardized laser irradiation areas, and offers a normalized metric for comparing non-equilibrium strength across varying laser spot sizes. As shown in Fig. 4(b), our experiment results for three different samples show that $|\psi_{OA}| \cdot \pi r_0^2$ increases with increased laser spot radius. This trend is consistently observed from all the WS_2 samples, apart from the result under the 50× objective lens in the as-grown monolayered WS_2 sample, where minor deviations are caused by measurement fluctuations. As described in our physical model before, photon absorption excites hot carriers that undergo ultrafast thermalization, followed by lateral diffusion out of the irradiation area. When the laser spot is large, the hot carrier diffusion length is much smaller than the spot radius, and most of the hot carriers remain within the beam area, leading to spatial confinement of energy and a correspondingly higher value of $|\psi_{OA}| \cdot \pi r_0^2$. However, for small laser spots, the carrier diffusion length becomes comparable to or exceeds the irradiation size. A significant number of hot carriers diffuse out of the irradiated region before transferring their energy to OPs. Consequently, the normalized parameter $|\psi_{OA}| \cdot \pi r_0^2$ decreases, highlighting the important role of lateral energy dissipation at small laser spot sizes.

In addition, $|\psi_{OA}| \cdot \pi r_0^2$ also varies across different material configurations. As shown in Fig. 4(b), under the same objective lens, the transferred monolayered WS_2 and the hetero-bilayered WS_2/WSe_2 have higher $|\psi_{OA}| \cdot \pi r_0^2$ values. This can be attributed to the presence of a tiny interface spacing under the WS_2 layer, which is introduced from the sample transfer process. Based on our past work,[23] such spacing modifies the local optical field, enhancing the optical absorption within the 2D material and thus resulting in a higher $|\psi_{OA}| \cdot \pi r_0^2$. Although the transfer of WS_2 leads to loosen interface coupling and may affect the cross-plane hot carrier diffusion,[24] we only consider the in-plane hot carrier diffusion here. This approximation does not compromise accuracy under our conditions, as all the WS_2 samples' thickness here (~0.7 nm) is much smaller than their optical absorption depth (tens of nm) and cross-plane hot carrier diffusion length (~μm). Therefore, the hot carrier population can be considered depth-uniform. Although some reports show that the existence of

ultrafast hot carriers transfer through hetero stacking interfaces;[25] in our case, the hot carriers will be rendered inside the 2D materials because of the density of state mismatch between WSe_2 and SiO_2.[26] However, when applying our FET-Raman method to multilayered or bulk materials, a cross-plane hot carrier diffusion model with depth-dependent generation, diffusion, and recombination kinetics needs to be considered. In addition, our FET-Raman can be applied to nanomaterials with different dimensions. The similar $\psi \sim 1/f$ relation and half of the CW case extrapolation limit are suitable for disparate materials. With similar profiles, it can be applied to evaluate the OA thermal non-equilibrium in single-walled carbon nanotubes,[22] supported few-layered MoS_2, and few-layered suspended graphene.[27]

In summary, we employed the FET-Raman method to effectively measure the OP–AP thermal non-equilibrium in supported monolayered WS_2. Our experimental results and analysis showed that the OP–AP thermal non-equilibrium was largely enhanced under localized heating. With the laser spot radius decreased from $\sim$1.7 to $\sim$0.4 μm, ψ_{OA}/ψ_{AP} increased by over 2.5 times for the three WS_2 materials. Also, the ψ_{OA}/ψ_{AP} discrepancy between hetero-bilayered WS_2/WSe_2 and monolayered WS_2 showed that the stronger van der Waals coupling may contribute to the diminishing OP–AP temperature difference. In addition, the hot carrier diffusion became more pronounced under small laser spots. As a result, $|\psi_{OA}| \cdot \pi r_0^2$ decreased by more than 60% after the laser spot radius decreased from $\sim$1.7 to $\sim$0.4 μm. Our study established a robust and precise experimental framework for probing phonon non-equilibrium in nanoscale materials, thereby providing pathways for understanding phonon transport and its implications for thermal management, nanoscale energy conversion, and high-performance electronic technologies.

See the supplementary material for details on sample preparation, structure characterization, the measured RSC under steady and transient states, and the RSC caused by OA thermal non-equilibrium and AP temperature rise.

Support for this work by the U.S. National Science Foundation (CBET No. 2425361, awarded to Wang) is gratefully acknowledged.

AUTHOR DECLARATIONS

Conflict of Interest

The authors have no conflicts to disclose.

Author Contributions

Yu Hua and Suman Jaiswal contributed equally to this work.

Yu Hua: Data curation (lead); Formal analysis (lead); Investigation (lead); Writing – original draft (lead). **Suman Jaiswal:** Data curation (lead); Formal analysis (lead); Investigation (lead); Methodology (lead); Writing – review & editing (equal). **Masoud Mahjouri-Samani:** Conceptualization (lead); Data curation (lead); Formal analysis (lead); Funding acquisition (lead); Investigation (lead); Methodology (lead); Project administration (lead); Resources (lead); Writing – review & editing (lead). **Xinwei Wang:** Conceptualization (lead); Data curation (equal); Formal analysis (equal); Funding acquisition (lead); Investigation (equal); Methodology (lead); Project administration (lead); Resources (equal); Software (lead); Supervision (lead); Writing – review & editing (lead).

DATA AVAILABILITY

The data that support the findings of this study are available from the corresponding authors upon reasonable request.

REFERENCES

[1]H. Song, J. Liu, B. Liu, J. Wu, H. Cheng, and F. Kang, Joule **2**(3), 442 (2018).
[2]S. A. bagherabad, M. Khanzadeh, and S. M. B. Marashi, Opt. Mater. **127**, 112249 (2022).
[3]S. Sullivan, A. Vallabhaneni, I. Kholmanov, X. Ruan, J. Murthy, and L. Shi, Nano Lett. **17**(3), 2049 (2017).
[4]R. Wang, H. Zobeiri, Y. Xie, X. Wang, X. Zhang, and Y. Yue, Adv. Sci. **7**(13), 2000097 (2020).
[5]D. K. Ferry, Appl. Phys. Rev. **8**(2), 021324 (2021).
[6]N. Hunter, N. Azam, H. Zobeiri, N. Van Velson, M. Mahjouri-Samani, and X. Wang, Adv. Mater. Interfaces **9**(7), 2102059 (2022).
[7]M. Rahbar, I. Al Keyyam, J. Liu, and X. Wang, Opt. Lett. **49**(17), 4971 (2024).
[8]S. Xu, N. Hunter, H. Zobeiri, H. Lin, W. Cheng, and X. Wang, Mater. Today Phys. **27**, 100816 (2022).
[9]I. A. Keyyam, B. Li, T. Wang, C. Deng, and X. Wang, Carbon **233**, 119906 (2025).
[10]N. Hunter, M. Rahbar, R. Wang, M. Mahjouri-Samani, and X. Wang, Opt. Lett. **47**(24), 6357 (2022).
[11]Y. Hua, I. Al Keyyam, Y. Xie, and X. Wang, J. Appl. Phys. **138**(1), 015104 (2025).
[12]B. Rehman, K. M. M. D. K. Kimbulapitiya, M. Date, C.-T. Chen, R.-H. Cyu, Y.-R. Peng, M. Chaudhary, F.-C. Chuang, and Y.-L. Chueh, ACS Appl. Mater. Interfaces **16**(25), 32490 (2024).
[13]K. Ni, J. Du, J. Yang, S. Xu, X. Cong, N. Shu, K. Zhang, A. Wang, F. Wang, L. Ge, J. Zhao, Y. Qu, K. Novoselov, P. Tan, F. Su, and Y. Zhu, Phys. Rev. Lett. **126**(2), 027402 (2021).
[14]P. Yuan, R. Wang, H. Tan, T. Wang, and X. Wang, ACS Photonics **4**(12), 3115 (2017).
[15]P. Yuan, R. Wang, T. Wang, X. Wang, and Y. Xie, Phys. Chem. Chem. Phys. **20**(40), 25752 (2018).
[16]N. Hunter, N. Azam, H. Zobeiri, R. Wang, M. Mahjouri-Samani, and X. Wang, ACS Appl. Mater. Interfaces **12**(45), 51069 (2020).
[17]Y. Zhang, Q. Lv, A. Fan, L. Yu, H. Wang, W. Ma, R. Lv, and X. Zhang, Nano Res. **15**(10), 9578 (2022).
[18]H. Zobeiri, R. Wang, Q. Zhang, G. Zhu, and X. Wang, Acta Mater. **175**, 222 (2019).
[19]N. Ansari, E. Mohebbi, and F. Gholami, J. Appl. Phys. **127**(6), 063101 (2020).
[20]Z. Lu, A. Vallabhaneni, B. Cao, and X. Ruan, Phys. Rev. B **98**(13), 134309 (2018).
[21]S. V. Koniakhin, O. I. Utesov, IN. Terterov, and A. V. Nalitov, Phys. Rev. B **95**(4), 045418 (2017).
[22]I. A. Keyyam, Y. Hua, B. Li, T. Wang, C. Deng, and X. Wang, Adv. Sci. **12**(37), e09005 (2025).
[23]N. Van Velson, H. Zobeiri, and X. Wang, Opt. Express **28**(23), 35272 (2020).
[24]F. M. Bartram, Y.-C. Leng, Y. Wang, L. Liu, X. Chen, H. Peng, H. Li, P. Yu, Y. Wu, M.-L. Lin, J. Zhang, P.-H. Tan, and L. Yang, npj Quantum Mater. **7**(1), 84 (2022).
[25]C. Sun, H. Zhou, T. Sheng, S. Li, and H. Zhu, ACS Nano **18**(1), 931 (2024).
[26]P. Yuan, H. Tan, R. Wang, T. Wang, and X. Wang, RSC Adv. **8**(23), 12767 (2018).
[27]H. Zobeiri, N. Hunter, R. Wang, T. Wang, and X. Wang, Adv. Sci. **8**(12), 2004712 (2021).